

Flow fields and droplet dynamics of turbulent spray flames in curved wall jet burner

M. S. Mansour^{1,2*}, I. Alkhesho¹, G. Scribano¹, H. Mitsudharmadi¹, F. Bisetti¹, S. H. Chung¹

¹Clean Combustion Research Center, King Abdullah University of Science and Technology, Thuwal 23955-6900, Kingdom of Saudi Arabia

²Department of Mechanical Engineering, Helwan University, Cairo, Egypt

ABSTRACT

A curved wall jet (CWJ) burner was employed to stabilize turbulent spray flames that utilize a Coanda effect; air is supplied as an annular-inward jet over a curved surface, surrounding an axisymmetric solid cone fuel spray. Flow velocity fields of the oxidizer and droplet size and velocity data were measured using Stereoscopic Particle Image Velocimetry (SPIV) and a Phase Doppler Interferometer (PDI) system, respectively. SPIV measurements revealed that the general features of the flow field exhibit typical flow characteristics of the CWJ burner. As the air flow rate increases, the droplets size (D_{32}) decreases upstream at off-center positions and becomes more uniform in the radial direction. Moreover, the mean axial droplets velocity reduces in the near-field flow of flames.

Introduction

Combustion of liquid fuel sprays impacts a variety of practical combustion devices such as gas turbines, compression-ignition engines, industrial furnaces and boilers [1]. Understanding the physical phenomena that control spray combustion processes is desirable, as most of these devices utilize the fuel in a two-phase flow. Phenomena such as flame stabilization, structure, and extinction are important aspects of spray flames that are not well understood across the wide variety of combustion systems. The mutual interaction of the spray and flow field can play an important role in determining the dominant mechanisms controlling flame behaviour i.e. flame stabilization and structures [2]. It is well-recognized that such interaction determines combustion efficiency and pollutant emissions [3].

There have been extensive experimental and numerical studies on turbulent spray combustion in different configurations [4]. The spray burner being investigated uses the Coanda effect [5] to create a configuration that improves flame stabilization and enhances droplet evaporation in the near-injector region. In a previous turbulent premixed flame study with the same burner [6], a mixture of propane/air was injected over a curved wall as a form of annular-inward jet. Due to the curvature of the streamlines, a low-pressure region was generated, resulting in flow adherence to the curved surface. As the static pressure recovered, the wall-jet separated to form a recirculation zone (RZ). The annular-inward jet collided over the RZ in an interaction jet region, generating a high level of turbulence by the collision as well as the effect of ambient air entrainment; this was subsequently developed as a merged jet in the downstream region. Such burner resulted in improved flame stabilization and a shorter flame length. Kim et al. [7] further improved premixed flame stabilization by modifying the burner with a cavity.

We propose a new burner concept that utilizes the aforementioned Coanda effect to stabilize turbulent spray flames. This was achieved by using a liquid fuel (n-heptane) that was injected through the spray nozzle at the centre of the burner as shown in Fig. 1. The evaporation of the liquid fuel is significantly augmented

due to the following: (1) The recirculated hot gases upstream enhance droplet evaporation significantly; (2) the air flow in the interaction jet region disperses the droplets; (3) the air entrainment associated with reactants or air flow dilutes the spray with oxidizer; (4) the steep velocity gradient, formed along the curved wall, enhances the interaction between the air and droplets.

Application of PIV [9] and PDI [10] techniques contributed to better understanding of spray-flow interaction. A turbulent ethanol spray flame was characterized using PDA in [11] in terms of droplet size and velocity. A comprehensive mapping of the flow and droplet fields in turbulent non-reacting and reacting dilute spray jets of acetone and ethanol fuels was presented in [12] utilizing an LDV/PDA setup. The flow field and droplet dynamics of spray flames were characterized using PIV and PDI measurements, respectively.

In the present study, we investigated the flow-spray-flame interactions close to the injection point of the burner with detailed spatial and temporal measurements using high-speed laser diagnostic techniques. Multi kHz stereo particle image velocimetry (SPIV) and Phase Doppler Interferometer (PDI) techniques were used to provide insight on turbulent non-reactive flow field and spray characteristics, respectively. This extensive database of high-resolution measurements is also required for turbulent spray combustion modelling.

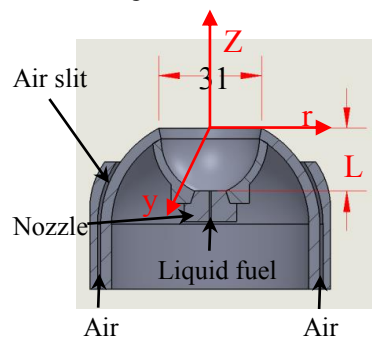


Figure 1 CWJ burner, all dimensions are in mm, $L = 5, 20$ mm.

* Corresponding author: morkous.abdo@kaust.edu.sa

Experiment and Diagnostics

I. The curved-wall jet burner

The CWJ burner (Fig. 1) is composed of an inner hollow cylinder with 70 mm in diameter and 150 mm in length, having a hemi-spherical end. On the top, the cavity has a width of 31 mm. A pressure assisted fuel injector (Danfoss) is inserted along the burner centreline. The distance from the injector tip to the burner exit plane, L , can be controlled, altering the residence time of the droplets inside the inner hollow cylinder and the flow-field-spray interaction region. In the present study, two values of L are investigated: 5 and 20 mm. The Danfoss solid cone nozzle is characterized by a 60° cone angle and 0.23 mm orifice. An outer flow guide has a concentric cylinder with 72 mm i.d.; this forms a converging section with an exit diameter of 56 mm and $R = 36$ mm. This converging section enables the velocity field to be directed tangentially into the curved surface then oriented toward the burner axis. This annular-inward jet collides in the jet interaction region, generating a high level of turbulence. We modified the dimensions of the concave cavity compared to [7] in order to accommodate a larger recirculation zone (RZ). The burner was mounted onto a 3D stepper motor-controlled traverse system that provides a spatial resolution of 0.62 mm.

Air was metered using mass flow controllers (BROOKS INSTRUMENT) and supplied through the curved-wall slit. Liquid fuel (>99% pure n-heptane) is supplied from a pressurized tank. The injection fuel pressure is varied between 4 and 11 bar. This corresponds to a fuel flow rate of 0.81 and 1.39 kg/hr. Details of test conditions are listed in Table 1. Case L5 (L20) marks the flame in which the pressure nozzle was placed at 5 (20 mm) upstream of the annular air jet as shown in Fig. 1. \dot{Q}_{air} is the air flow rate and \dot{m}_f is the fuel mass flow rate that is kept constant in the current study at 1.247 kg/hr corresponding to 9 bar fuel pressure. ϕ is the liquid fuel equivalence ratio. The characteristic Reynolds number, $Re = d_{eff} V_0 / \nu_a$, is based on the mean jet velocity, V_0 , the kinematic viscosity of air, ν_a , calculated from Gaseq code [13] and the effective diameter, d_{eff} , defined as $d_{eff} = (4A_0/\pi)^{0.5}$, where A_0 is the exit area at the slit, which is calculated from the normal projection from the tip of the outer cylinder to the inner one. The exit area was kept constant at 200 mm² in the present study and Re ranges from 0 to 17520. Several parameters in Table 1 will be further discussed later.

Table 1 Details of experimental conditions.

Case	\dot{Q}_{air} [Lpm]	\dot{m}_f [kg/hr]	ϕ	Re
L5-1	0		-	0
L5-2	60		4.32	5256
L5-3	200		1.30	17519
L20-1	0	1.247	-	0
L20-2	60		4.32	5256
L20-3	200		1.295	17519

II. Stereoscopic Particle image velocimetry (SPIV)

The SPIV system (LaVision, LDY 300) consists of a high-repetition rate (up to 10 kHz) twin-cavity diode-pumped Nd:YLF laser (Litron, LDY304-PIV at 527 nm, 28 mJ/pulse, 5 ns pulse duration) and two CMOS cameras (LaVision, Imager Pro HS 4M with 2016×2016 pixels) coupled with a high speed controller. A laser sheet of about 1 mm thickness and 90 mm height was formed using two cylindrical lenses. A time separation of 30 to 50 μ s was used at 2.5 kHz, producing 3D vector fields every 0.4 ms.

Seed particles were TiO₂ having 0.18 μ m nominal diameter. Seed levels were adjusted for accurate vector computation and maintained the number of spurious vectors during image processing below 5%. The Mie scattered light from each laser pulse was recorded on a separate frame. The two cameras were placed equidistant from, and on the same side of, the laser sheet to collect forward and backward scattered light at an angle of 40° with the laser sheet plane. The Scheimpflug mounts had an angle of $5-7^\circ$ to project the focus plane onto the target frame. Two different apertures were used to match recorded light intensity for the two cameras to compensate for the intensities of the forward and backward scattered light. Distortion from the camera system was remedied by imaging a 3-D dot target (LaVision type 11).

The velocity vector fields were determined through a multi-pass vector computation technique (LaVision Davis 8.1 software) with interrogation region size of 32×32 pixels having 50% overlap, equivalent to a spatial resolution of 1.1×1.1 mm. The system was operated at 2.5 kHz and 0.2 s of flow times were recorded such that 500 double-frame images were analyzed.

III. Phase Doppler Interferometer (PDI)

A 2D Phase Doppler Interferometer (PDI) system was used to characterize spray droplets size and velocity distributions as well as the number density. The system measures the velocities in z and r coordinates shown in Fig. 1. The PDI allows the simultaneous measurement of droplet velocity and size, where the droplet size is determined based on the measured phase shift difference between two Doppler bursts whilst the droplet velocity is derived from the Doppler burst frequency. The PDI system (model 300 MD, Artium Technologies) consists of a continuous solid laser that produces two continuous laser beams at 532 and 491 nm. The former has 350 mW power to measure the axial velocity component (V_z) and droplet size, while the latter has 100 mW power to measure the radial velocity component (V_r). Four beams were split and focused by a 150 mm focal length lens to form a measurement probe volume. The light scattered from droplets passing through the measurement volume was captured by the receiving optics positioned at $\theta=45^\circ$ off axis in the forward scattering mode to maximize the collection of light as shown in Fig. 2. The focal length of the receiving optic was 350 mm.

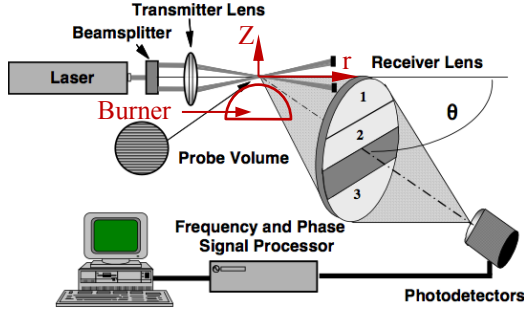


Figure 2 Schematic of the PDI.

Three photomultiplier detectors are lined up and are maintained at a fixed separation from each other. The three photomultiplier tubes convert the three light signals from the three detectors into three electronic signals that are processed to extract velocity and size information. The signals from the photomultipliers are post processed by 2 ASA post processors. One processor is used for the z component of the velocity and size, whereas the other processor is used for the r component of the velocity. The measured size is corrected for the probe volume correction according to the Gaussian beam effect [14]. The droplets size statistics are based on the corrected size distribution.

Results and Discussion

1. Non-reacting flow field characteristics

The SPIV system was used to characterize the turbulent flow field for a non-reacting condition. A coordinate system is adopted in representing data with (r,z,y) in the radial, axial and normal coordinates, respectively, with $z=0$ at the tip of the cavity (Fig. 1). Data collected from 500 images at 2.5 kHz were analyzed and the mean velocities (V_r , V_z , V_y) and rms velocities (V_r' , V_z' , V_y') in the radial, axial and normal coordinates, respectively, were determined. The spatial distributions of (V_r , V_z), together with color-coded magnitude of V_y are shown in Fig. 3 for the non-reacting flow conditions that mimic cases (L5-2(L20-2), L5-3(L20-3)).

The non-reacting flow field exhibits flow characteristics similar to those of the CWJ burner. The flow field consists of a recirculation zone (RZ), an interaction jet (IJ) region with the collision of the annular-inward jets near $z=10$ mm, and a downstream merged jet (MJ) region. Inner and outer shear layers (ISL and OSL) surrounding the annular-inward jets (AJ) can also be identified as shown in Fig. 3.

The axial (at $r=0$) and radial (at $z=4$ mm) profiles of the mean and rms velocities are plotted in Fig. 4 for the non-reacting flow conditions that correspond to Fig. 3. The recirculation zone is clearly exhibited by V_z having negative values for $0 < z < 10$ mm (Fig. 4a), which approaches 4 m/s (case L5-3 or L20-3). In the interaction jet region, V_z increases rapidly and then decreases slightly up to $z=90$ mm in the merged jet

region. V_r exhibits higher values near $z=15$ mm in the interaction jet region. However, cases L5-1 or L20-1 reveal negligible value of V_r (see Fig. 4b).

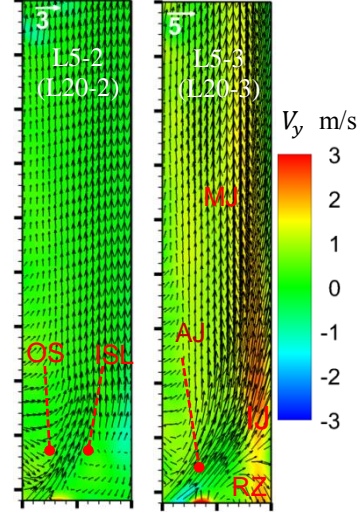


Figure 3 Spatial distribution of mean velocity fields with the background color indicating the y -velocity component for the non-reacting flow conditions corresponding to L5-2(L20-2) and L5-3(L20-3) cases.

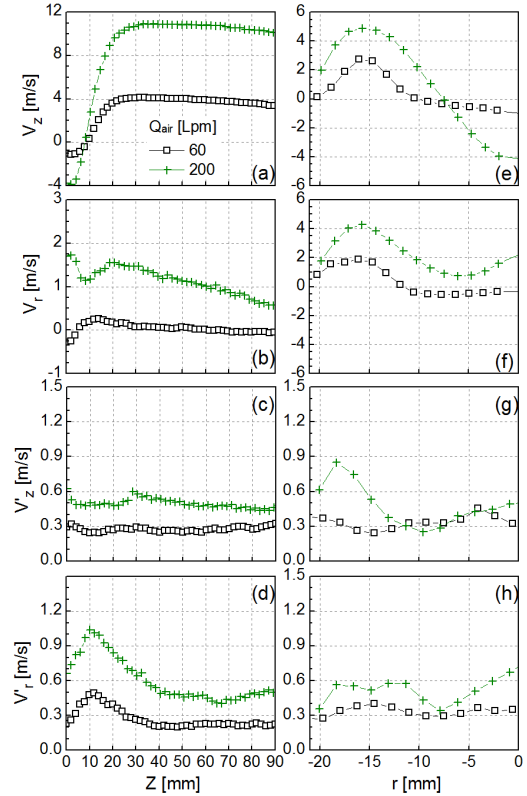


Figure 4 Axial V_z (a), V_r (b), V_z' (c) V_r' (d) and radial V_z (e), V_r (f), V_z' (g) V_r' (h) profiles of mean and rms velocities for the cases in Fig.3.

The axial profiles of rms velocities (Figs. 4c, and 4d) show that V_r' is high in the RZ and reaches its maximum in the interaction jet region, while it is spatially uniform in the merged jet region. V_z' is spatially homogeneous also. These results indicate that the collision of annular-inward jet near the boundaries of RZ influences the generated turbulence.

The radial profiles of V_z (Fig. 4e) at $z=4$ mm again exhibit RZ (negative values), inner and outer shear layers (large velocity gradient), and annular-inward jets. V_z and V_r peak near $r=15$ mm in the annular jet region. V_r decreases at the centreline and in the outer shear layer.

The outer shear layer plays a more important role than the inner shear layer in generating high values of all rms velocity components, particularly in high Re flames as shown in Fig. 4(g). However, V_r' exhibits relatively high values at $r=0$ in case L5-3 (L20-3) due to the collision of the annular-inward jets. These rms velocities are expected to be influenced significantly by the heat release in reacting flames [15].

II. Droplets velocity and size in flames

The radial profiles of axial and radial mean velocities (left axis) of n-heptane fuel droplets for reacting cases L5-1 and L5-3 are shown in Fig. 5 at two different axial locations ($z=4, 12$ mm). The corresponding rms velocities are shown on the right axis. These values for case L20 are shown in Fig. 6. It is shown that the profiles of the mean axial velocity of the droplets in the near-field flow of n-heptane flames is slightly (significantly) lower than in the spray without annular air for $L = 5$ mm ($L=20$ mm). In flames without the air jet, droplets exhibited higher values of velocities because there is no a recirculated flow; however, as we introduced the annular air jet, the droplets display low and even negative velocities at the centerline that is reversed near the spray-air shear layer for case L5. The peak axial and radial droplet velocities shown in Figs. 5 and 6 are lower than the corresponding local mean gas velocities close to the centerline reported in Fig. 4. This is attributed to the drag effect on the droplets by the recirculated gases momentum. RMS velocity components exhibit higher values with air particularly downstream of flame L20-3. Values of V_r' and V_z' increase radially and have high magnitudes within the shear layers.

The Sauter mean diameter (D_{32}), representing the droplet size, is shown in Fig. 7 under reacting conditions for cases L5-1(L20-1) and L5-3 (L20-3). The mean droplet sizes generally increase radially due to droplet inertia augmented by the created flow field; such trend is consistent with previous results in a swirling spray flame [16]. The series of cases L20 show lower droplet sizes since further downstream from the spray injection point, the effect of evaporation and reaction on droplet sizes is more pronounced. The annular air-jet influences significantly the droplet size, particularly within both the recirculation zone and the interaction jet region. As the air flow rate increases, the droplets size decreases upstream at off-center positions; such effect is less apparent toward the burner centerline. Along the centerline, the effect is reversed. As L increases, the droplets size becomes more uniform moving outward radially, particularly downstream ($z=12$ mm); similar trends are observed for the cases L5 upstream ($z=4$ mm).

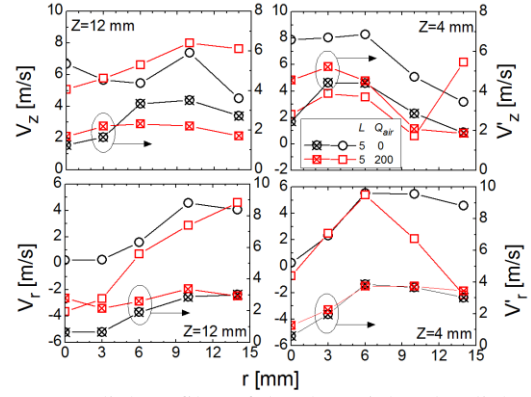


Figure 5 Radial profiles of droplet axial and radial mean velocities (left) and the corresponding rms values (right) for two different heights (z) of cases L5-1 and L5-3.

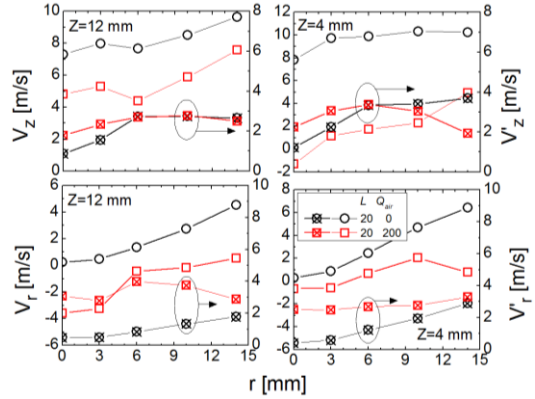


Figure 6 Radial profiles of droplet axial and radial mean velocities (left) and the corresponding rms values (right) for two different heights (z) of cases L20-1 and L20-3.

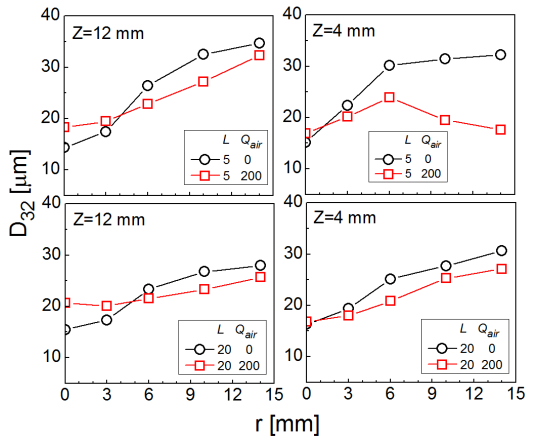


Figure 7 Radial profiles of D_{32} for two different heights (z) of cases L5-1 (L20-1) and L5-3 (L20-3).

III. PDFs of droplets in flames

Although droplet mean velocities and D_{32} provide information on the overall interaction of the n-heptane spray with the annular air flow field, no information is provided on the dynamics of individual droplets. Such information is obtained in the form of the velocity distribution and droplet size pdfs. The radial profiles of probability density functions (pdfs) of the velocity distributions for flames L5-1, L5-3, L20-1 and L20-3 are shown in Figs. 8 and 9 at $z=4$ mm while the axial

profiles are shown in Fig. 10 at $r=0$. Results indicate that profiles of velocity distribution change significantly with location in the flame.

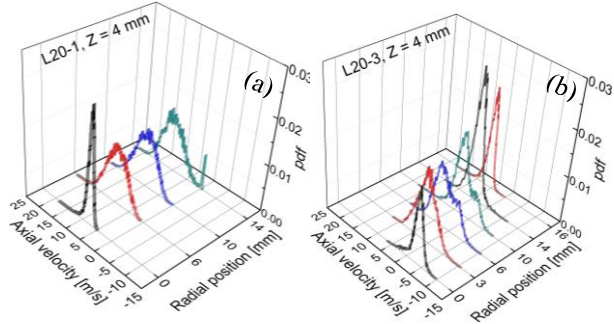


Figure 8 Radial distribution of axial velocity pdf at $z=4$ mm for cases (a) L20-1 and (b) L20-3.

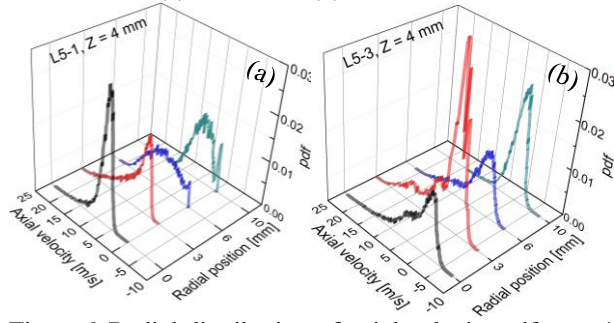


Figure 9 Radial distribution of axial velocity pdf at $z=4$ mm for cases (a) L5-1 and (b) L5-3.

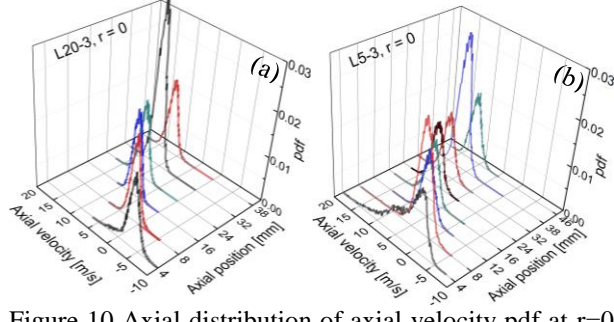


Figure 10 Axial distribution of axial velocity pdf at $r=0$ for cases (a) L20-3 and (b) L5-3.

Most of the velocity distributions shown are monomodal and negative velocities are present within the RZ of cases L5-3 (L20-3) due to the momentum of recirculated gases. The presence of a wide range of positive and negative droplet velocities is indicative of the influence of the current burner aerodynamics on droplets dynamics [14]. These distributions resemble lognormal distributions and have a tail to the higher velocities and a relatively steep drop at the lowest velocities. The majority of droplets are found at lower velocities in cases L5-3 and L20-3 compared with L5-1 and L20-1 due to the influences of recirculated gases particularly at small radii. The axial profiles shown in Fig. 10 reveal that the nozzle position (L) influences velocity distributions significantly. This is attributed to the mutual interaction between the spray and the surrounding air flow field particularly within the RZ.

Radial distributions of droplet size measured in the reacting spray jets are shown in Figs. 11 and 12 for

spray cases L20 and L5 respectively at $z=4$ mm, exhibiting the dramatic effect of annular air. The axial distributions are shown in Fig. 13 at $r=0$. Spray flames with introducing the annular air display a clear shift of the peak of the distribution towards smaller droplet sizes and the flatness of the distribution generally increases with air far from the injection point. Such decrease in size with increasing air flow may be attributed to the existence of secondary atomization in the spray jet. Also, the flatness of these pdfs is more pronounced downstream as shown in Fig. 13 revealing a uniform droplet size distribution that probably appears to improve the flame stabilization. It is possible that turbulence is contributing to such trends. It is notable that, for case L5-3, the size distributions are uniform across the jet exit plane.

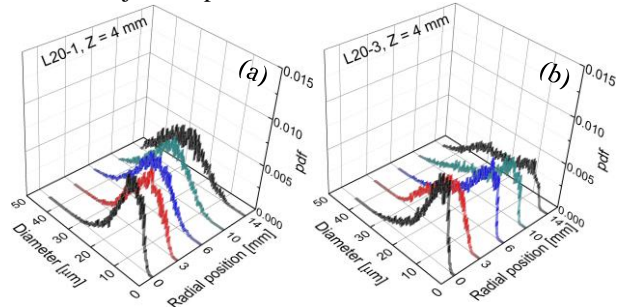


Figure 11 Radial distribution of droplets size pdf at $z=4$ mm for cases (a) L20-1 and (b) L20-3.

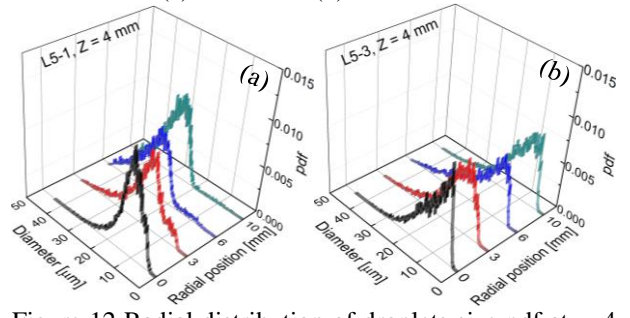


Figure 12 Radial distribution of droplets size pdf at $z=4$ mm for cases (a) L5-1 and (b) L5-3.

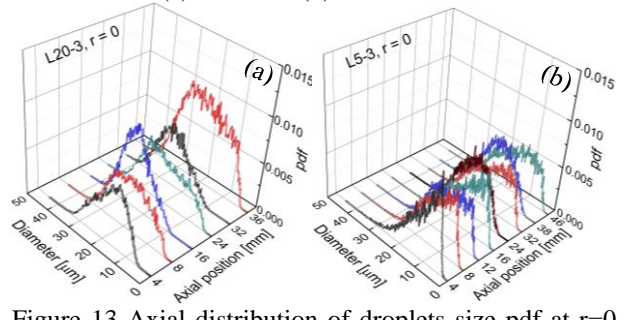


Figure 13 Axial distribution of droplets size pdf at $r=0$ for cases (a) L20-3 and (b) L5-3.

The joint distributions of droplet velocity and size are shown in Fig. 14 for L5-1, L5-3, L20-1 and L20-3 cases at two different axial ($z=4, 12$ mm) and radial ($r=0, 14$ mm) positions. Generally, the surrounding annular air jets contributes to disperse the droplets significantly. Cases without air jets reveal that large droplets possess high positive velocities as axial velocity increases with

the droplet size. However, introducing annular air around the spray improved the evaporation/atomization of large droplets as large droplets disappear (see Fig. 14) particularly for L20 cases.

At $z=4$ mm, air jets reduce the velocities of small droplets and numerous droplets are recirculated within the recirculation zone as shown in Fig. 14 (upper row). However, at $z=12$ mm, droplets are located within the interaction jet region, which contributes to disperse droplets with positive axial velocities particularly at $r=14$ mm. Again the droplet size increases with the radial position for cases without air jets. The number density of the droplets for flame L5-1 is low at $r=14$ mm and $z=4$ mm; however, introducing the annular air jets disperses these droplets radially increasing the number of droplets through the PDI probe volume.

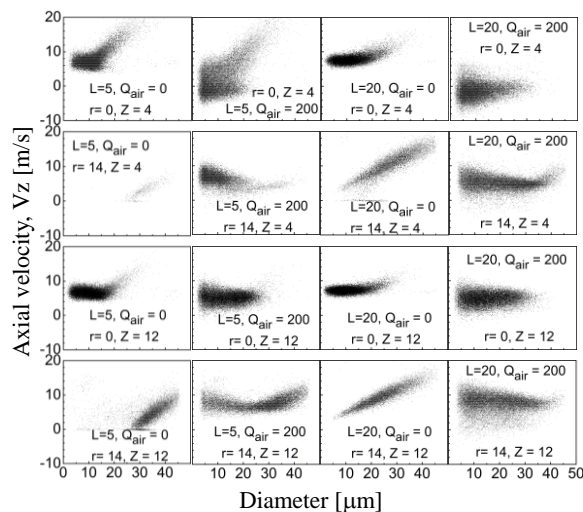


Figure 14 Droplet size-velocity correlation at two different radial ($r=0, 14$ mm) and axial ($z=4$ and 12 mm) spatial positions for flames L5-1, L5-3, L20-1 and L20-3.

Conclusions

The interaction of spray and air stream in n-heptane turbulent spray nonpremixed flames was investigated to obtain a comprehensive mapping of the flow and droplet fields in turbulent non-reacting jets and reacting spray flames. A curved wall jet (CWJ) burner was employed to stabilize turbulent spray flames. The burner utilized a Coanda effect by supplying air as annular-inward jet over a curved surface, surrounding an axisymmetric solid cone fuel spray. Stereoscopic particle image velocimetry (SPIV) quantified the flow field features while phase Doppler interferometer (PDI) was used to characterize droplet dynamics. We investigated the effects of increasing the oxidizer (air) flow rate at a fixed liquid flow rate and the position of fuel atomizer with respect to the annular-inward jet (L) on the spray characteristics. SPIV measurements revealed that the general features of the flow field exhibit typical flow characteristics of the CWJ burner; a recirculation zone (RZ) near the cavity exit, an interaction jet (IJ) region with the collision of the annular-inward jets near $z=10$

mm, and a downstream merged jet (MJ) region. Also, high turbulent rms velocities were generated within the recirculation zone, which improved the flame stabilization. As the air flow rate increased, the droplets size decreased remarkably upstream at off-center positions; such effect diminished toward the burner centerline and finally was reversed along the spray centerline. It is also found that as the annular air jet is supplied, large droplets are vaporized/atomized and then dispersed. As L increases, the droplets size becomes radially more uniform. It is shown that the profiles of the mean axial droplets velocity in the near-field flow of n-heptane flames is slightly (significantly) lower than in spray without annular air for $L=5$ mm ($L=20$ mm).

References

- [1] Faeth, G. M., Prog. Energy Combust. Sci. 13 (1987) 293-345.
- [2] Faeth, G. M., Prog. Energy Combust. Sci. 9 (1983) 1-76.
- [3] Lefebvre, A. H., American Institute of Aeronautics and Astronautics, 12 (1984) 887-898.
- [4] Faeth, G. M., "Spray combustion phenomena", Proc. Comb. Inst. 26 (1996) 1593-1612.
- [5] Gregory-Smith, D. G., Hawkins, M. J., Int. J. Heat and Fluid Flow, 12 (1991) 323-330.
- [6] Gil, Y. S., Jung, S. H., Chung, S. H., Combust. Flame, 113 (1998) 348-357.
- [7] Kim, D., Gil, Y. S., Chung, T. W., Chung, S. H., Combust. Sci. and Tech. 181 (2009) 1397-1412.
- [8] Kohse-Höinghaus, K., Jeffries, J., Applied Combustion Diagnostics, Taylor & Francis, New York, 2002.
- [9] Chong C.T. and Hochgreb S., Fuel 115 (2014) 551-558.
- [10] Strakey, P. A., Talley, D. G., Sankar, S. V., and Bachalo, W. D., Applied Optics, Vol. 39 (2000) No. 22.
- [11] Duwel, I., Ge, H.-W., Kronmayer, H., Dibble, R., Gutheil, E., Schulz, C., Wolfrum, J., Proc. Combust. Inst. 31 (2007) 2247-2255.
- [12] Gounder, J. D., Kourmatzis, A., Masri, A. R., Combust. Flame, 159 (2012) 3372-3397.
- [13] Morley C., Gaseq chemical equilibrium program available at: c.morley@ukgateway.net
- [14] Bachalo, W. D. and Houser, M. -J. AIAA-84-1199 (1984).
- [15] Hartung, G., Hult, J., Kaminski, C. F., Rogerson, J. W., Swaminathan, N., Physics of Fluids, 20 (2008) 035110.
- [16] Presser C., Gupta A. K., Semerjian H. G., Combust. Flame 92 (1993) 25-44.